Supplement S1 - Control and stability of flows, RH, temperature, and droplet size distributions

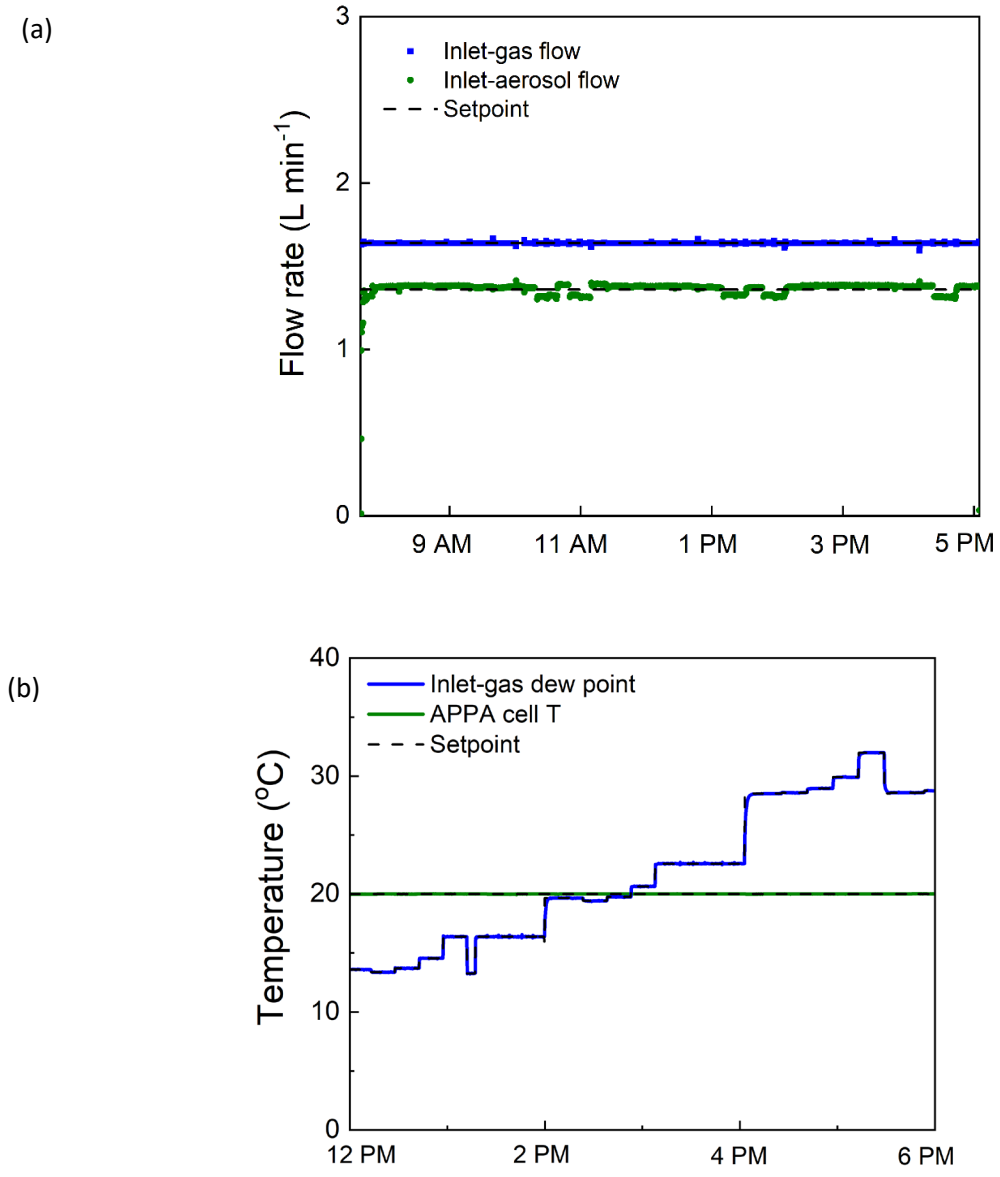

Figure S1. Example of control over several hours of (a) the inlet-gas and inlet-aerosol flow rates and (b) the temperature of the reactor and dew point of the inlet-gas flow. The steps in the inlet gas dew point reflect changes in the humidified air flow rate, which themselves result from changes in the flow rate from the O_3 generator. The inlet-aerosol flow dew point is assumed to always be 14.5 °C, which was determined experimentally using the approach described in the text.

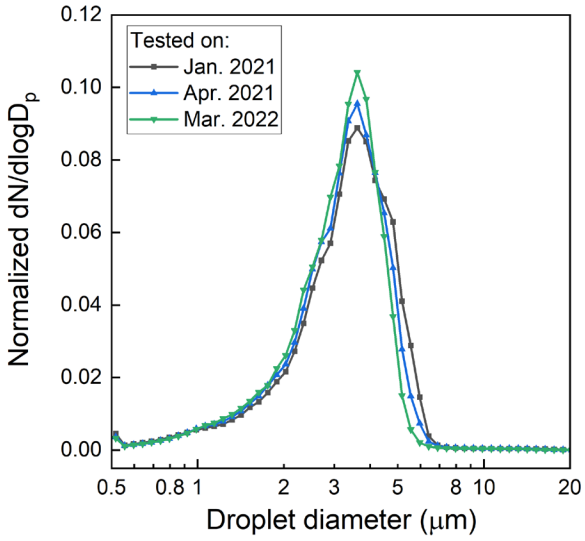

Figure S2. Consistency of the droplet size distribution measured at the outlet of the APPA over more than one year.

Supplement S2 - Approach used to control RH in reactor

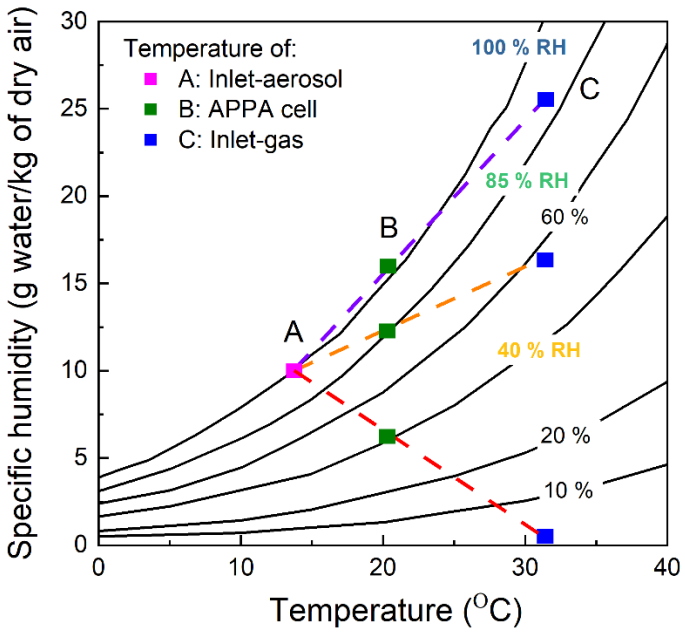

Figure S3. Relationship between the temperature and water vapor content of the two inlet flows and the resulting RH in the reactor.

Supplement S3 - Sulfate formation in droplet phase

Figure S4 shows an example of the dry size distributions measured at the outlet of the APPA by the SMPS for an experiment in which the cloud droplets formed on injected 0.04 μm seed particles. Ozone was injected during both measurements, while SO_2 was for only the experiment resulting in the red distribution in the figure. The small mode to the right of the main peak corresponds to particles having two elementary charges when separated by the DMA shown in Figure 2 in the main text, and that subsequently lost one of those charges in the neutralizer downstream of it. The separation between the singly-charged and doubly-charged particle modes decreases accompanying the formation of sulfuric acid in part because the mass added to both modes is the same, which causes a greater relative change in size for the smaller singly-charged particles than the larger doubly-charged ones. The dry particle mode diameter increased from 0.040 μm to 0.051 μm.

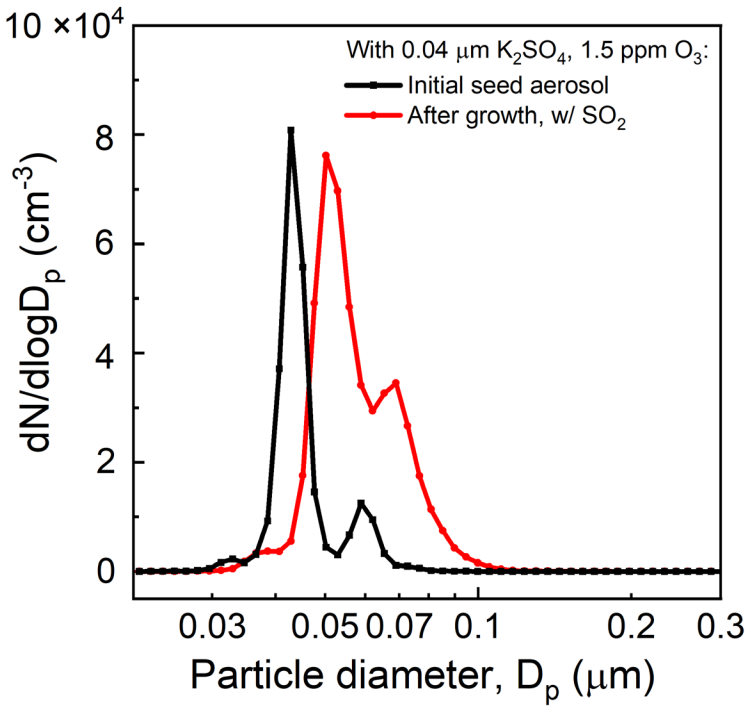

Figure S4. Dry particle number size distributions of the initial K_2SO_4 seed particles (black) and of the cloud-processed particles exiting the reactor (red) that had grown as dissolved SO_2 was oxidized by O_3 to form aerosol-phase sulfuric acid.

Supplement S4 – UV and visible spectrum inside the reactor when illuminated with the xenon lamp

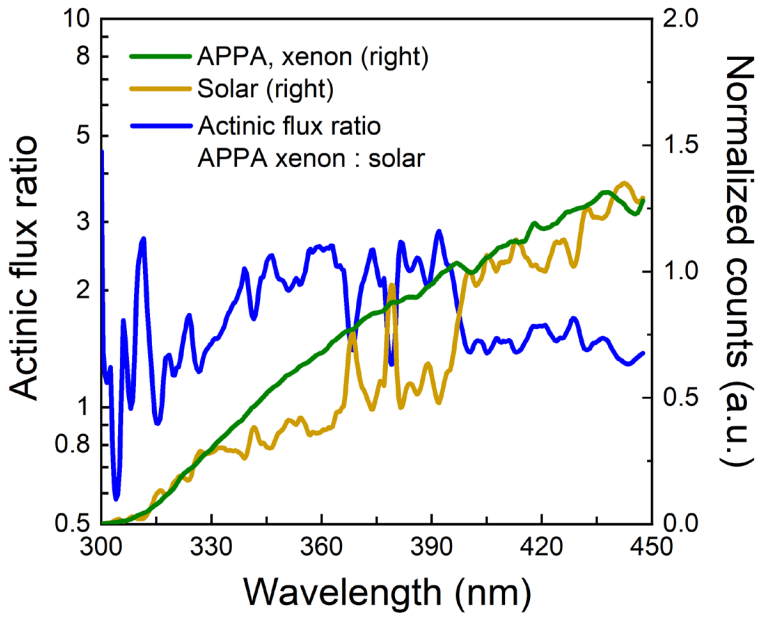

Figure S5. Spectral actinic fluxes inside the reactor when illuminated by the xenon lamp (green curve) and outdoors around noon on a sunny day in April (yellow curve), and the wavelength-dependent ratio of the two (blue curve). The approach used to calculate actinic flux from spectral irradiance measured with a spectrometer is described in the text.

Supplement S5 – OH exposure determined from SO_2 and benzene oxidation experiments

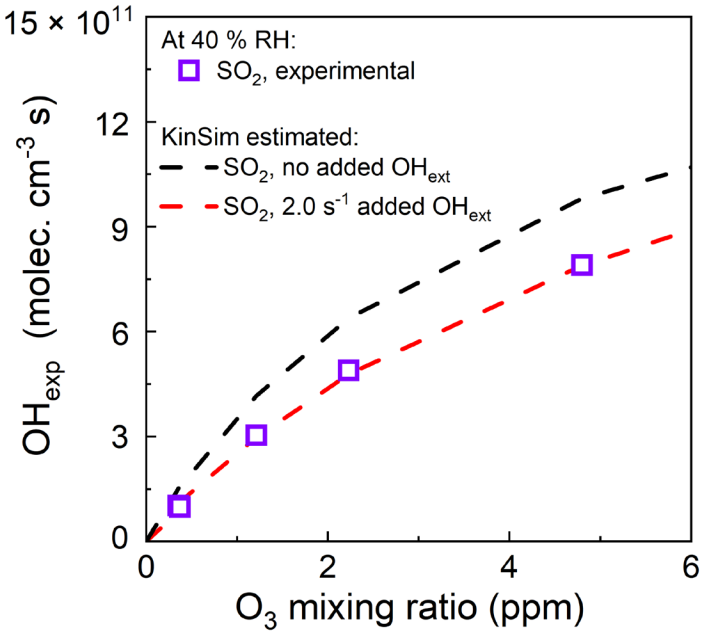

Figure S6. Variation of OH_{exp} estimated from SO_2 decay as a function of initial O_3 mixing ratio for 40 % RH.

The OH_{exp} values calculated from measurement of the reactive loss of benzene for RH = 40 % RH (dry seed particles), 85 % RH (aqueous seed particles), and 100 % RH (cloud droplets) are presented as the markers in Figures S7 (a), (b), and (c), respectively. Whereas the sulfuric acid resulting from the oxidation of SO_2 by one OH radical does not undergo any subsequent reaction with OH, oxidation of most organics results in a multi-generation cascade of products that are also reactive with OH. The upper curves in Figure S7 represent OH_{exp} from KinSim simulations in which OH reacts only with the added benzene, while the lower curves are from simulations in which OH also reacts with the first-generation oxidation products with a reaction rate constant of 10x that of OH reaction with benzene. Reaction of 1st and higher generation oxidation products is expected to increase with increasing OH concentration, resulting in the sort of downward shift in experimentally determined OH_{exp} towards and beyond the lower curve with increasing O_3 concentration (and OH production). Additional reaction of oxidation products in the aqueous

phase may explain the slightly greater downward shift in data in Figure S7 (c) for the 100 % RH experiments. Based on the comparisons of the experimental and simulation OH_{exp} for all of the SO_2 and benzene experiments, a reasonable estimate of uncertainty in the OH_{exp} estimated from KinSim is approximately ±20 %.

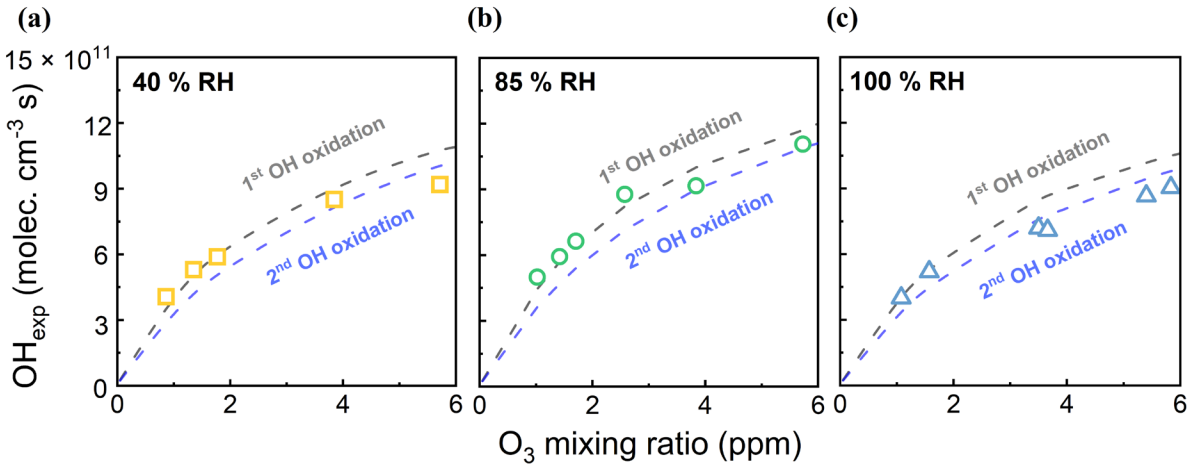

Figure S7. Variation of OH_{exp} as a function of initial O_3 mixing ratio for **(a)** low RH mode (40 %) **(b)** high RH mode (85 %) and **(c)** cloud mode (100 %).

Supplement S6 – SOA composition from toluene oxidation

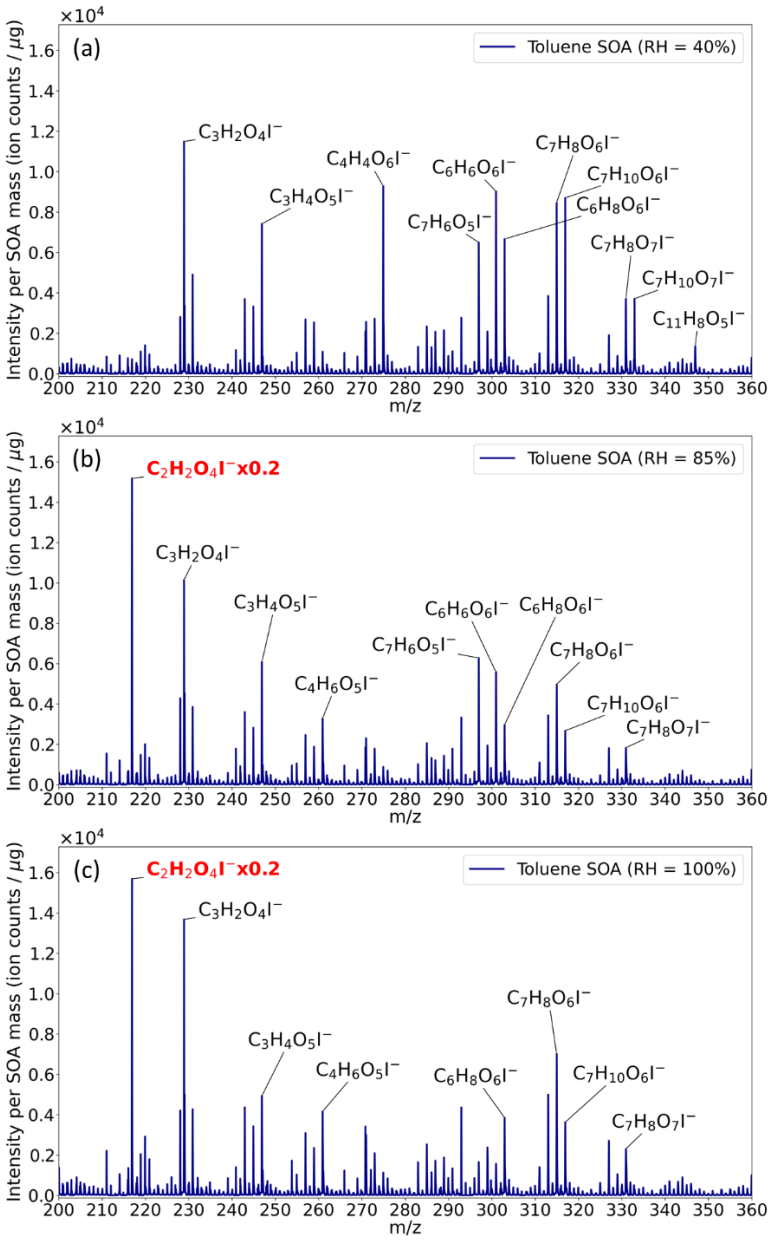

Figure S8. Mass spectra of SOA produced from OH-oxidation of toluene in the presence of dry seed particles (40 % RH), aqueous seed particles (85 % RH), and cloud droplets (100 % RH), with OH exposures calculated from KinSim of 1.06×10^{12}, 1.03×10^{12}, and 1.01×10^{12} molec. cm^{-3} s, respectively. The aerosol was collected on PTFE membrane filters and then evaporated from a FIGAERO inlet connected to an HR-ToF-CIMS. A peak corresponding to oxalic acid ($C_2H_2O_4$) was dominant for both the 85 % RH and 100 % RH cases but absent for the 40 % RH case (note that the amplitudes of the oxalic acid peaks in both the 85 % and 100 % RH spectra were multiplied by 0.2).

Supplement S7 – Cycling of reactor RH during measurement of secondary aerosol formation in ambient air

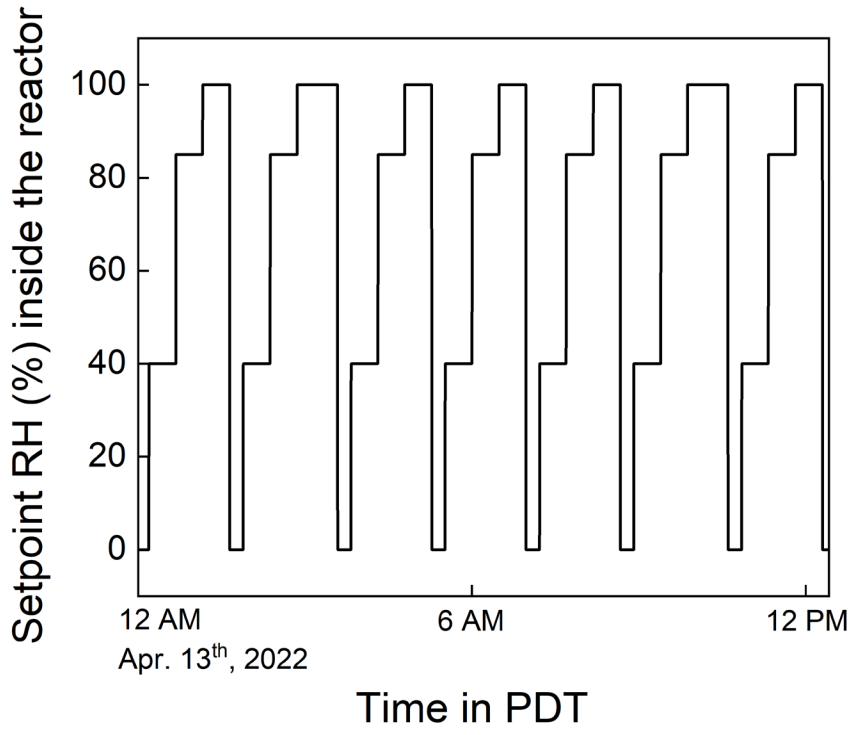

Figure S9. A typical RH cycle showing steps in the sequence of 40 %, 85 %, and 100 % RH. The short periods with very low RH follow the 100 % RH measurements and are designed to evaporate any residual liquid water from the walls before the start of the next 40 % RH measurement.

Table S1. Aqueous-phase reactions added to the KinSim "OFR radical chemistry" module. The rate constants are effective values used to express the rates as if the reactions occur in the gas-phase per cm^3 of air in the reactor. They were calculated for an LWC of 0.3 g m^{-3} and with the assumption that aqueous phase concentrations are described by Henry's Law.

No.	Reaction	Effective rate constant (cm^3 $molec^{-1}$ s^{-1})
R1	$OH + HO_2 \rightarrow H_2O + O_2$	8.37×10^{-11}
R2	$OH + O_3 \rightarrow HO_2 + O_2$	5.29×10^{-17}
R3	$HO_2 + HO_2 \rightarrow H_2O_2 + O_2$	5.22×10^{-11}
R4	$OH + H_2O_2 \rightarrow HO_2 + H_2O$	7.87×10^{-12}
R5	$HO_2 + O_3 \rightarrow 2O_2 + OH$	7.65×10^{-15}
R6	$OH + CO_2 \rightarrow HCO_3$	1.3×10^{-18}